Shake Table Test on Seismic Response of a Precast Frame with Recycled Aggregate Concrete

Jianzhuang Xiao[1,*], Thi Loan Pham [1, 2] and Tao Ding [1]

[1]Department of Structural Engineering, Tongji University, 1239 Siping Road, Shanghai 200092, PR China
[2]Department of Civil Engineering, Haiphong University, 171 Phan Dang Luu Road, Haiphong 180000, Vietnam

(Received: 6 March 2014; Received revised form: 4 April 2015; Accepted: 19 April 2015)

Abstract: A precast frame model made of Recycled Aggregate Concrete (RAC) was constructed with precast beams, columns and Cast-In-Place (CIP) joints. Then a shaking table test was carried out with three types of earthquake ground motions, namely Wenchuan, El Centro and artificial Shanghai waves. Based on the shaking test, structural responses such as dynamic characteristics, cracking and failure pattern, seismic responses as well as the overall seismic performance of the model were analyzed and evaluated. The results indicate that the precast RAC frame structure has an adequate load bearing potential as well as ductility against moderate and severe seismic excitations. Therefore, the perfect combination of RAC and precast structures is feasible to apply and popularize precast RAC frame structures with mid-rise buildings in the seismic regions.

Key words: recycled aggregate concrete (RAC), precast, frame, shake table test, seismic response.

1. INTRODUCTION

Although concrete is currently the most widely applied engineering material in the world, it has emitted a huge carbon footprint into the air. More specifically, recent statistics indicate that the prevalent uses of this material in the world contribute to 5 percent of annual anthropogenic global CO_2 emissions, of which China's booming construction industry alone occupies 3 percent. With an increasing number of the demolitions of existing buildings due to the urbanization process, a large amount of waste concrete is produced. In addition, natural disasters such as earthquakes also significantly contribute to the abundance of the waste concrete. Therefore, recycling waste concrete is probably deemed a sound and effective solution to preserve natural resources, to protect environment and to deal with massive construction and demolition wastes.

Since the study on fundamental behaviors of recycled aggregate concrete (RAC) is well-documented in the current literature, its mechanical properties are accordingly explored (Bhikshma and Kishore 2010; Limbachiya 2004; Lo 2008; Fonseca 2011; Xiao *et al.* 2012). For instance, the compressive, tensile and shear strengths of RAC are generally lower than those of Natural Aggregate Concrete (NAC); the modulus of elasticity for RAC generally reduces as the content of Recycled Coarse Aggregate (RCA) increases; the RCA replacement percentage has nearly no influence on the bond strength between RAC and deformed rebars. In addition, the properties of RAC are greatly influenced by the mix proportion (Parekh and Modhera 2011) and it is clearly known that mixing concrete will be controlled much better in factory conditions. Therefore, the authors suggest that RAC components can be produced in precast factories in order to take inherent advantages of precast elements and ensure the quality of construction (Xiao *et al.* 2012). Prefabrication of building elements in a factory condition brings with its

*Correspondence author. E-mail: jzx@tongji.edu.cn; Fax: +86-21-65986345; Tel: +86-21-65982787.

certain inherent advantages over purely site-based construction. For instance, speed, quality and efficiency, they are all cited as specific attributes of precast construction. Noticeably of all these attributes, speed is the most highly considered (Nakaki *et al*. 1999).

Along with mechanical properties of RAC, many studies on the structural performance of RAC have also been conducted such as beams (Xiao *et al*. 2013; Zhang *et al*. 2006; Andrzej 2011), columns (Xiao *et al*. 2012; Andrzej 2011), beam-column joints (Xiao *et al*. 2010; Corinaldesi 2011), slabs (Zhou *et al*. 2008) and plane frames (Xiao *et al*. 2006). The positive results of these studies further support and strengthen the possibilities of applying RAC in civil engineering structures. However, the current literature on RAC reveals that most of the studies focus on monolithic (wholly cast-in-situ) structures and the topics of earthquake response of precast RAC structures seem to be ignored. Therefore, the dearth of studies on the latter topic is a motivation for this paper to be conducted. The current study aims to investigate the seismic response of a precast RAC frame structure subjected to earthquake excitations.

Precast concrete structures made of NAC are widely used in many countries, especially in the United States, New Zealand, and Japan where moderate-to-severe earthquakes often occur. Observing from some earthquake events recently, such as Kobe earthquake in Japan in 1995 and Christchurch earthquake in New Zealand in 2011, the on-site reports and observations of damage to reinforced concrete buildings indicated that both cast-in-place and precast concrete frame structures performed similarly under earthquake attack by the means of capacity design and proper connection detailing of the precast concrete elements (Elwood *et al*. 2012; Shariatmadar and Beydokhti 2011).

The seismic performance of precast concrete structure depends on the ductility capacity of the connectors jointing each precast components, especially at critical joints such as the beam-to-column connections. Therefore, the development of the seismic connections is essential in the precast construction. The detail and location of precast concrete connections have been the subjects of numerous experimental and analytical investigations (Alcocer *et al*. 2002; Xue and Yang 2010; Xiao *et al*. 2010; Ericson 1995; Shutt 1995). Most of the precast concrete constructions adopt connection details emulated Cast-In-Place (CIP) concrete structures so that they should have equivalent seismic performance as monolithic concrete members. For instance, the failure patterns, strengths and drift ratios as well as ductility were satisfied in comparison with monolithic specimens in those researches.

Therefore, a 6-story precast RAC building has been constructed using CIP concrete made of recycled coarse aggregate (RCA) to complete the joints between precast components in order to investigate earthquake response by the shaking table test.

The contents of the current study are first to present the construction process of the world's first precast space frame structure made of RAC. Then structural dynamic characteristics (i.e., natural frequency, vibration modes, stiffness and damping ratios), visual damage observation (i.e., cracking and failure pattern), earthquake actions (i.e, seismic force, story shear), deformation (i.e., maximum story displacement and inter-story drift) and relationships between force and deformation (i.e., capacity curve and hysteretic loop) will be intensively explored, analyzed and discussed. As a result, a comprehensive understanding of the seismic behavior of RAC will be revealed, particularly the overall earthquake response of the precast RAC frame structure.

2. RESEARCH SIGNIFICANCE

In order to take the inherent advantages of precast construction and improve quality of elements in structures made of RAC, the earthquake response of a precast RAC space frame structure has been investigated. The results reveal the overall dynamic behaviors of the precast frame structure made of RAC and accumulate the experimental evidence for establishing related design guidelines for such structures made of RAC constructed in earthquake areas. The precast RAC structure constructed with CIP concrete joints indicates the ability of competition with monolithic construction and develops application of RAC in civil engineering as a structural material since acquiring knowledge of dynamic nonlinear earthquake responses of precast frame structures made of RAC.

3. SHAKING TABLE TEST PROGRAM

3.1. Recycled Coarse Aggregate

Recycled coarse aggregates (RCA) were produced from aged concrete that has been demolished, as shown in Figure 1. Most of the cube compressive strength for demolished concrete is ranged from 20 MPa to 40 MPa.

Recycled aggregates can be produced in plants similar to those used to crush and screen conventional natural aggregates. Large protruding pieces of reinforcing bars are first removed by hydraulic shears and torches. Then a jaw crusher is often selected for primary crushing because it can handle large pieces of concrete and residual reinforcement. Jaw crushers also fracture a smaller proportion natural aggregate in the parent concrete. The residual reinforcement is removed by large electro-magnets. Impact crushers are preferred for secondary crushing as they produce a higher percentage of aggregate without adhered mortar. In general the shape of recycled aggregate is rounder and less flaky

Figure 1. Demolition concrete produced RCA of model

Figure 3. Recycled coarse aggregate of tested model

than natural aggregate, as shown in Figure 2.

Due to the scale factor of the tested model, RCA was sieved in the range from 5–10 mm as shown in Figure 3. The measured apparent density of the RCA was 2481 kg/m^3 and the water absorption was 8.21%.

Figure 2. Processing plant

3.2. Precast RAC Frame Model

The tested model was designed by scaling down the geometric from prototype structure and the dimension scaling parameter was taken as 1:4 due to the limitation of shake-table parameters of the State Key Laboratory for Disaster Reduction in Civil Engineering at Tongji University. The model was designed with Chinese Standard GB50010-2002 code and the beam-column joints were cast-in-place based on emulation approach (Park 1986; Ericson and Warnes 1990; Mujumdar *et al*. 2001; Thomas *et al*. 2003). Based on dimensional analysis-Buckingham's Pi theorem (Buckingham 1914; Sabnis *et al*. 1983) and similitude requirements for dynamic loading, the variables that govern the behavior of vibrating structures reveals that in addition to length (l) and force (F), which are considered in static load situations, now the time (t) must be included as one of the fundamental quantities. Therefore, it is logical to choose S_l, S_E and S_a. The remaining scale factors are then calculated and given in Table 1. It is well-known that the shaking table test is conducted on the earth, so the gravity acceleration applied in the model and

Table 1. Similitude factors between the prototype and the test model

Item	Parameter	Formula	Relationship	Remark
Geometry	Length	S_l	**0.25**	Control the dimension
	Displacement	$S_\delta = S_l$	0.25	
	Elastic modulus	S_E	**1.00**	
	Stress	$S_\sigma = S_E$	1.00	Control the material
Physics	Poisson's Ratio	$S\upsilon$	1.00	
	Strain	$S_\varepsilon = S_\sigma/S_E$	1.00	
	Mass density	$S_\rho = S_\sigma/S_a\, S_l$	2.165	
	Mass	$S_m = S_E S_l^2/S_a$	0.034	
Load	Area load	$S_p = S_\sigma$	1.00	
	Concentrated force	$S_F = S_E S_l^2$	0.063	
	Period	$S_t = S_l^{1/2}/S_a^{1/2}$	0.368	
Dynamic characteristics	Frequency	$S_f = S_l^{-1/2}/S_a^{-1/2}$	2.719	
	Velocity	$S_v = S_l^{1/2}.S_a^{1/2}$	0.680	
	Acceleration	S_a	**1.848**	Control the shaking table test
	Acceleration of gravity	S_g	1.00	

prototype are the same (Zhang 1997; Andreas *et al.* 2010). So the similarity coefficient of gravity acceleration equals 1. Based on the similarity coefficient, the time interval of original seismic waves was scaled by 0.368.

The recycled aggregate concrete mixture of nominal strength grade C30 was proportioned with the recycled coarse aggregates (RCA) replacement percentage equal to 100%. The mix proportion is water: cement: sand: RCA = 1:1.859:3.202:4.554. The fine iron wires of 8# (diameter of 3.94 mm) and 10# (diameter of 3.32 mm) were adopted as the longitudinal reinforcement and 14# (diameter of 2.32 mm) for transversal reinforcement in this model. The measured average mechanical properties of the fine iron wires are presented in Table 2.

The tested model was a two-bay, two-span and six-story frame structure regular in elevation. The RAC frame model was 2175 × 2550 mm in plan and had a constant story height of 750 mm. Column sections were square with 100 mm depth. The beams were 125 mm depth by 50 mm width, cast monolithically with a 30 mm deep slab. The beams were doubly reinforced at the top and bottom. The details of the general geometry, the element sections and the corresponding reinforcements of the precast beams and columns in both X and Y-directions are shown in Figures 4(a)-(d).

Table 2. Mechanical properties of reinforcement

Specifications	Diameter (mm)	Yield strength (MPa)	Ultimate strength (MPa)	Elastic modulus (GPa)
8#	3.94	358	407	200
10#	3.32	306	388	200
14#	2.32	252	363	200

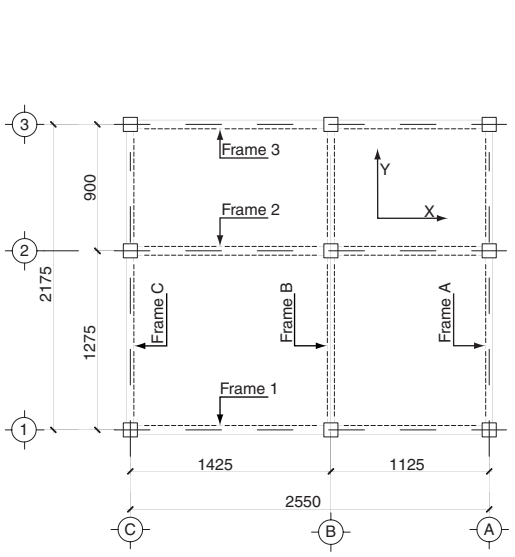

(a) Plan view

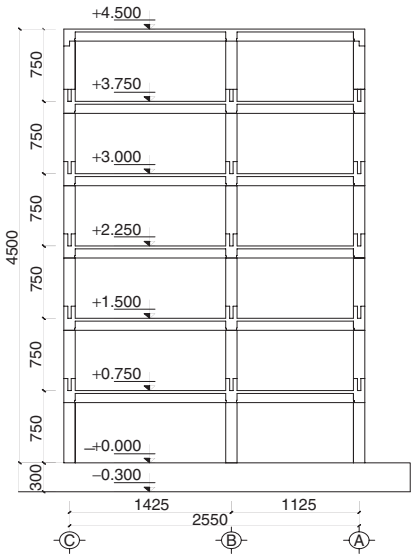

(b) Elevation view

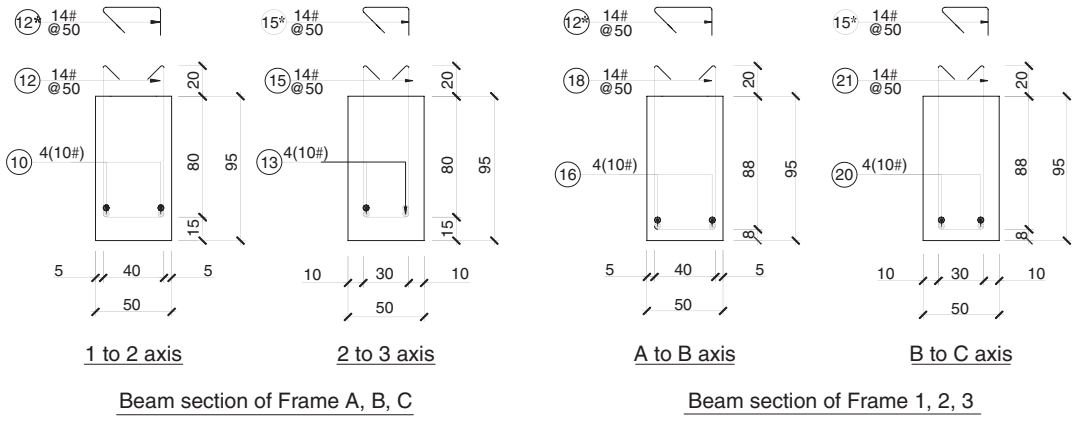

(c) Reinforcement of beam sections

Figure 4. (*Continued*)

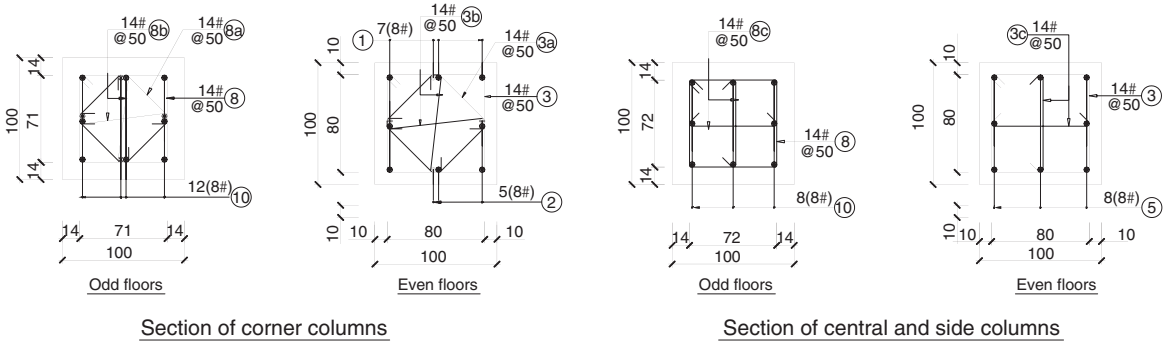

(d) Reinforcement of column sections

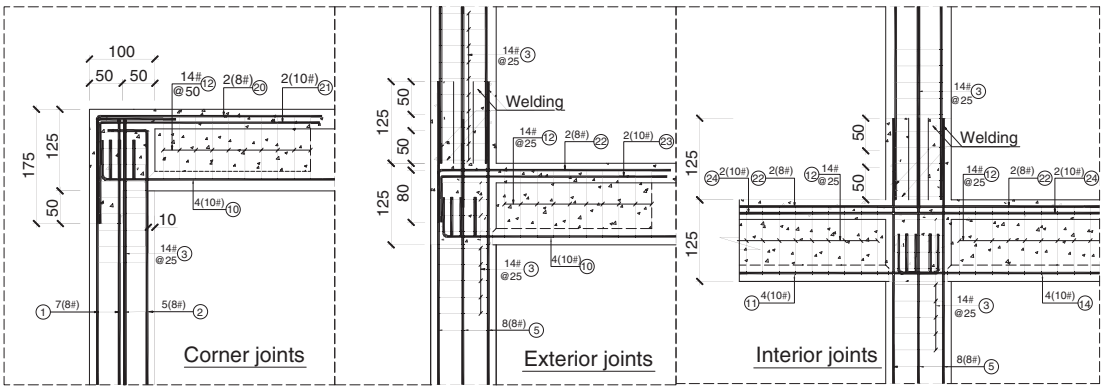

(e) Details of joints

Figure 4. Configuration and reinforcement of the model (Unit: mm)

The details of the reinforcing bars in the beam-column joints by the front view are shown in Figure 4(e).

An additional mass of 1528 kg was uniformly distributed to each slab from the 1st to 5th floors, and 1375 kg to the roof with iron blocks and plates to simulate mass density and loading conditions based on calculation by similarity coefficient presented in Table 1. The total mass of the model was estimated to be 17000 kg including the base beams, which was less than the capacity limitation of the shaking table.

3.3. Fabrication and Construction of the Model

The process of producing the model included two stages: (1) fabricate beam and column elements in a factory, and (2) construct the precast model in the lab. The precast RAC elements consisted of 54 columns and 72 beams. The fabrication process was the same for two types of components. Firstly, reinforcing bars of both components were assembled into the reinforcing cages. Then the reinforcing cages were placed into the wooden forms which were coated with form oil. All components were ready for pouring as presented in Figures 5(a)-(d). Ready-mix recycled concrete grade of C30 was casted for all the specimens. The specimens were cured at the ambient temperature for 28 days and transported to the construction site in the lab.

Single story columns were erected at each floor level and the beams were seated on the head of columns by beam rear. The continuity of longitudinal reinforcement through the beam-column joint was designed and connected by welding to ensure rigid beam-column connections. Three typical joints of the model were captured in Figure 6. With this method of precast construction, the model was erected one floor at a time with beams placed at the head of columns on the one level floor before the columns of the upper level floor were erected, then two layers of slab reinforcement were fixed in the forms, and RAC was cast-in-place for the joints and slabs. The process of construction is shown step by step in Figure 7.

3.4. Instruments

In order to measure the acceleration and displacement which are considered as basic data for the interpretation and analysis of test results, the instruments were set up on the model. As shown in Figure 8, a total of 30 accelerometers were installed, with 2 on the ground floor on both the X and Y-directions, 4 on each floor from the 1st to the 5th floor, and 8 on the roof. A total of 14 displacement Linear Variable Differential Transducers (LVDTs) were installed, with 2 on each floor from the 1st to the 5th in both X and Y-directions,

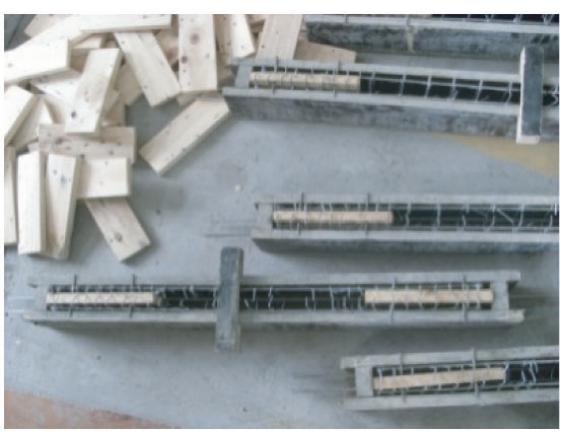

(a) Beam forms

(b) Precast beams

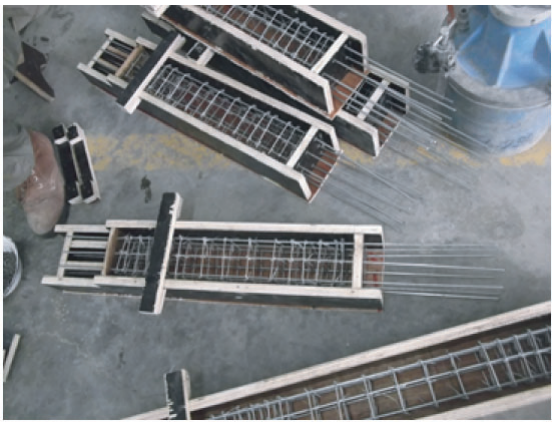

(c) Column forms

(d) Precast columns

Figure 5. Process of fabrication precast elements

(a) Corner joint

(b) Side joint

(c) Central joint

Figure 6. Configuration of joints assembled

(a) Lay up precast RAC beams and columns

(b) Welding rebars of joints

(c) Pouring RAC for joints and slabs

Figure 7. Process of construction

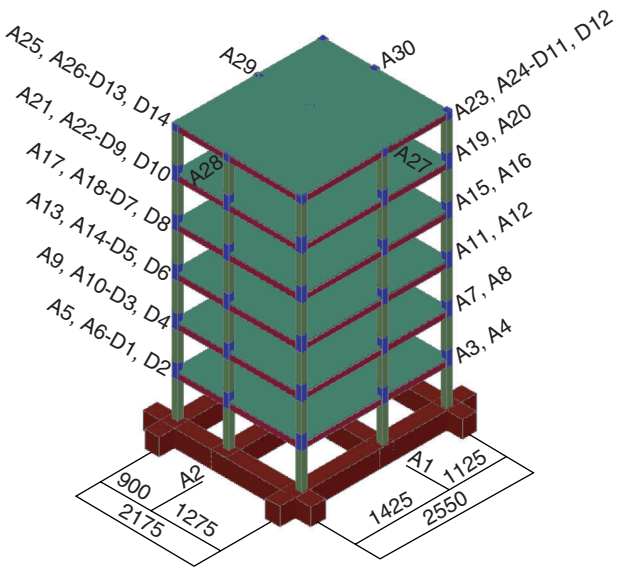

Figure 8. Arrangement of accelerometers and displacement LVDTs

and 4 on the roof. The arrangements of the instruments are illustrated in Figure 8. After that, the model ready for test was captured as shown in Figure 9.

3.5. Seismic Wave and Loading Program

According to the GB 50011-2010 (2010), Wenchuan seismic wave (WCW, 2008, N-S) and El Centro wave (ELW 1940, N-S) should be considered for Type-II site soil. The time history of WCW is shown in Figures 10(a)-(d). Considering the spectral density properties of Type-IV site soil, Shanghai artificial wave (SHW) were selected as shown in Figures 10(e)-(f), respectively.

The test program consisted of 8 phases, that is, tests

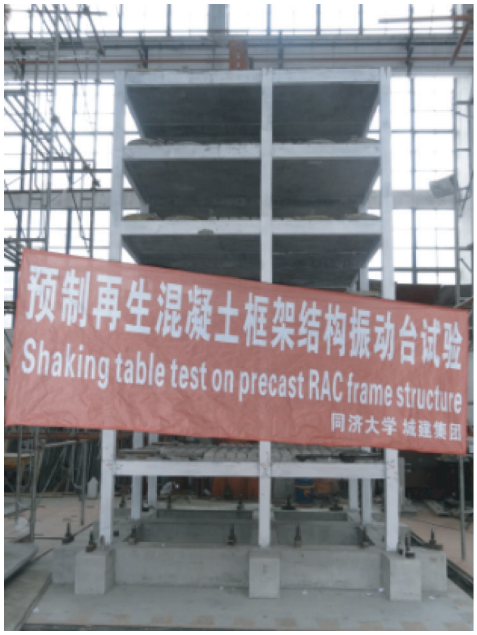

Figure 9. General view of precast RAC frame model

for Peak Ground Acceleration (PGA) of 0.066 g, 0.130 g (frequently occurring earthquake of intensity 8), 0.185 g, 0.264 g, 0.370 g (moderately occurring earthquake of intensity 8), 0.415 g, 0.550 g, 0.750 g (rarely occurring earthquake of intensity 8) were set to evaluate the overall capacity and investigate the dynamic response of the precast RAC frame structure. WCW, ELW and SHW were inputted in sequence during the test process. After each level of ground acceleration were input in the X-direction, a white noise was scanned in both X and Y-directions to determine the natural frequencies and the damping ratios of the model structure. And in this case, the peak value of the white-noise input was designed as 0.05 g. The detailed test information is presented in Table 3.

4. TEST RESULTS AND ANALYSIS

4.1. Cracking and Failure Pattern

Based on observing the progress of cracking after each test phase and the final state of the model, the cracking propagation and width of cracks were recorded throughout the shake table test with gradually increasing PGA amplitude of input motions. During the elastic stage with PGAs from 0.066 g to 0.130 g, no visible cracks appeared. Since the precast model stepped into the cracking stage with PGAs from 0.185 g to 0.370 g, the cracks on the beams of the 1st and 2nd floor, were clearly seen and propagated quickly. There were also some cracks at the foot of columns of the 2nd floor with the crack width around 0.1 mm. The test phases with PGAs from 0.415 g to 0.750 g indicated the damage and failure stage because the appearance of long and wide cracks as well as the crushing of concrete was found, which denoted relative obvious and serious damage. In particular, the first diagonal cracks appeared at joints of 1st and 2nd floor and the width of crack at the end of the beam reached 2 mm. Vertical flexural cracks appeared at the ends of beams on the 3rd floor and cracks at the top of columns also emerged. The circuit cracks at the foot of the 1st floor columns were clearly seen with the crack width around 0.5 mm. Besides, long cracks on the corner slab were also seen clearly and the noise of cracking could be heard. It indicates that the damage was contributed to all components of the structure so the precast model was able to withstand rarely occurring earthquake with PGA of 0.750 g. The typical cracks occurred on the precast RAC model after the tests are displayed in Figure 11.

The crack pattern of joints in precast frame made of RAC is relatively similar to that of precast frame made of NAC which were investigated by many researchers, such as Alcocer *et al*. (2002) and Xue and Yang (2010) as presented in Figure 12.

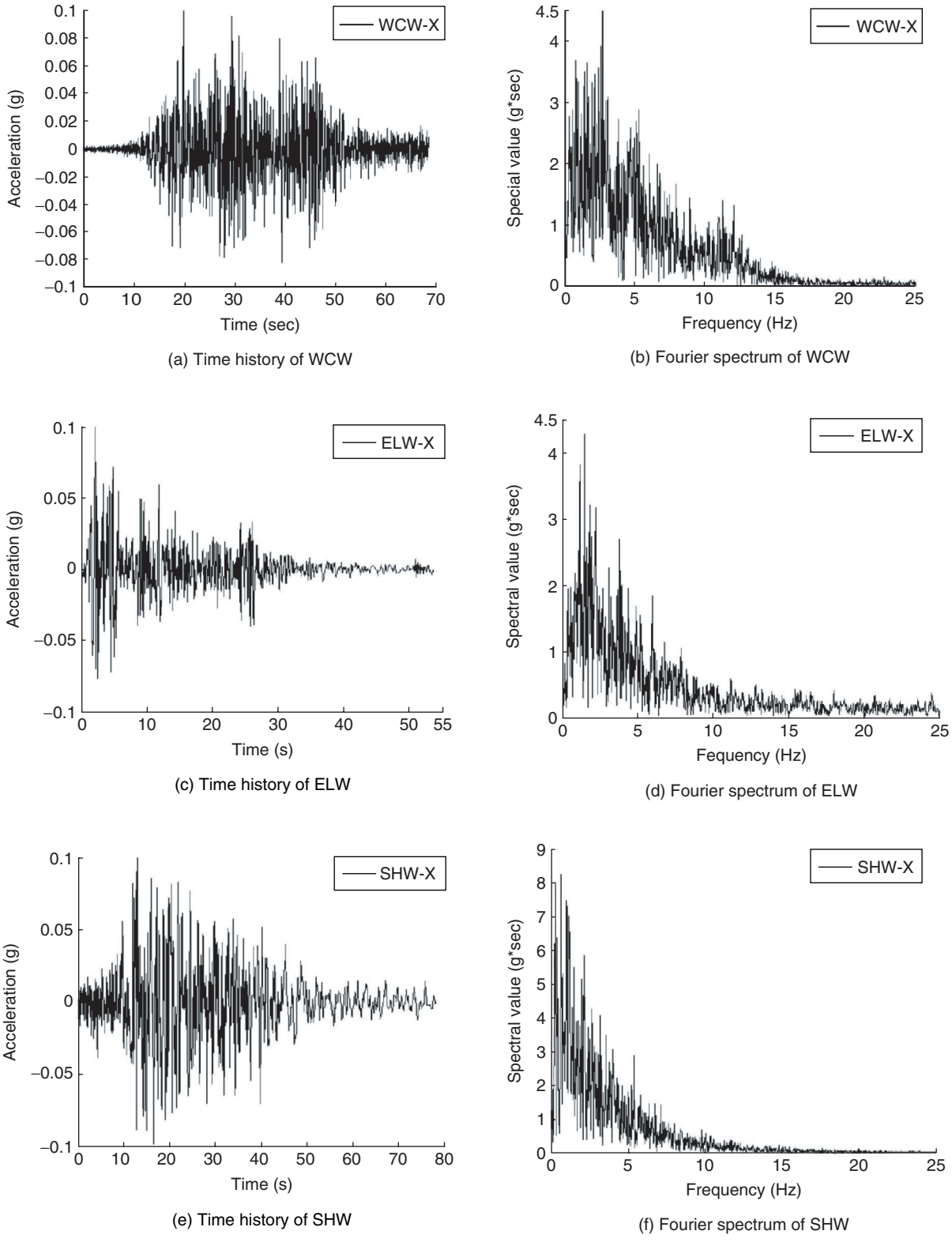

Figure 10. Earthquake input motions (the PGA s of original waves were scaled to 0.1 g)

4.2. Dynamic Characteristics

The dynamic characteristics of the structure are considered to be the natural frequency/period, stiffness, mode shape and damping. Using the experimental results in terms of the ground acceleration and the accelerations of the six stories of the frame model, the natural frequencies of the model in various modes were determined and the mode shapes were also obtained. The stiffness of the model is calculated by following formula:

Table 3. Loading program

		PGA (g)					PGA (g)		
		X-direction					X- direction		
No.	Input	Designed	Measured	Variation (%)	No.	Input	Designed	Measured	Variation (%)
1	White noise	0.050	0.032	–36.00	18	WCW	0.370	0.374	1.08
2	WCW	0.066	0.075	14.09	19	ELW	0.370	0.349	–5.68
3	ELW	0.066	0.067	1.21	20	SHW	0.370	0.278	–24.86
4	SHW	0.066	0.068	2.58	21	White noise	0.050	0.036	–28.00
5	White noise	0.050	0.037	–26.40	22	WCW	0.415	0.443	6.75
6	WCW	0.130	0.139	7.31	23	ELW	0.415	0.440	6.02
7	ELW	0.130	0.135	3.85	24	SHW	0.415	0.438	5.54
8	SHW	0.130	0.146	12.00	25	White noise	0.050	0.034	–31.20
9	White noise	0.050	0.037	–26.00	26	WCW	0.550	0.595	8.18
10	WCW	0.185	0.231	24.86	27	ELW	0.550	0.548	–0.36
11	ELW	0.185	0.197	6.49	28	SHW	0.550	0.561	2.00
12	SHW	0.185	0.175	–5.41	29	White noise	0.050	0.035	–30.00
13	White noise	0.050	0.036	–28.00	30	WCW	0.750	0.744	–0.80
14	WCW	0.264	0.273	3.41	31	ELW	0.750	0.766	2.13
15	ELW	0.264	0.261	–1.14	32	White noise	0.050	0.036	–28.00
16	SHW	0.264	0.269	1.89	33	SHW	0.750	0.679	–9.47
17	White noise	0.050	0.035	–30.00	34	White noise	0.050	0.036	–28.00

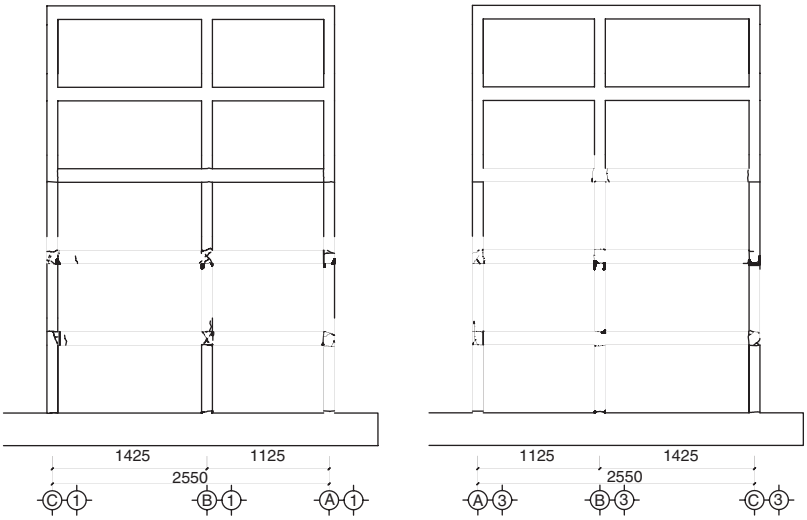

(a) Crack pattern of Frame 1 (b) Crack pattern of Frame 3

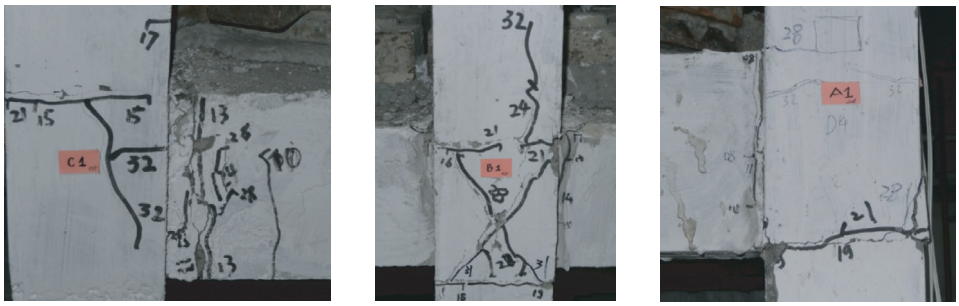

(c) Left exterior joint (d) Interior joint (e) Right exterior joint

Figure 11. Typical crack pattern of the precast RAC frame

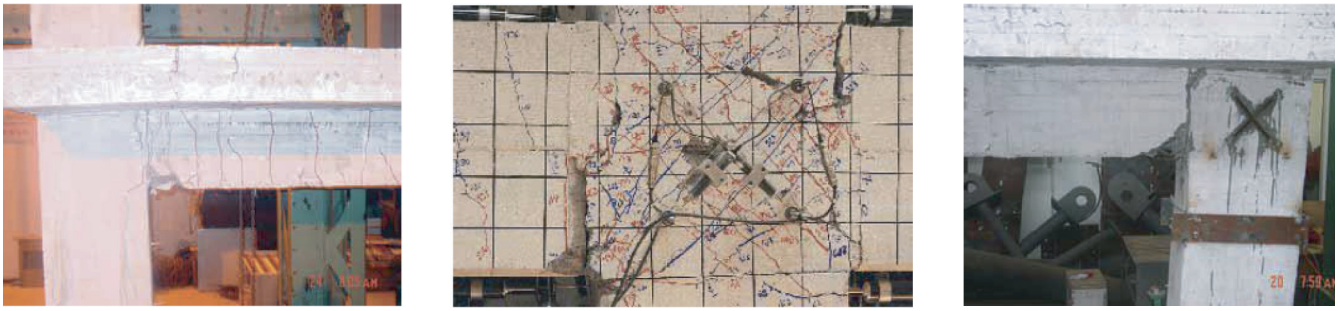

Figure 12. Typical crack pattern of the precast NAC frame (Alcocer *et al.* 2002; Xue and Yang 2010)

$$K = (2\pi f)^2 M, \tag{1}$$

where, K is the stiffness; f is the natural frequency; and M is the mass of the model.

Then the stiffness ratio is expressed by:

$$\frac{K_i}{K_0} = (\frac{f_i}{f_0})^2, \tag{2}$$

where, K_0 and f_0 are the initial stiffness and natural frequency respectively; K_i and f_i are the stiffness and natural frequency conducted by white noise after each earthquake level i^{th}, respectively.

The results show that frequencies of vibration steadily decrease with gradually amplitude increasing of motion in the X-direction as presented in Figure 13. The well-known half-power bandwidth method was used to calculate the equivalent viscous damping ratios. However, this method is appreciated in case of the damping ratio far less than one, so in the later test phases the results are not precise due to the high damping ratio of the model in the nonlinear range. Thus, the values of damping ratios which are extremely high in the later test phases are presented herein only as references. The damping ratios increase more rapidly in the X-direction in the later test phases as given in Table 4.

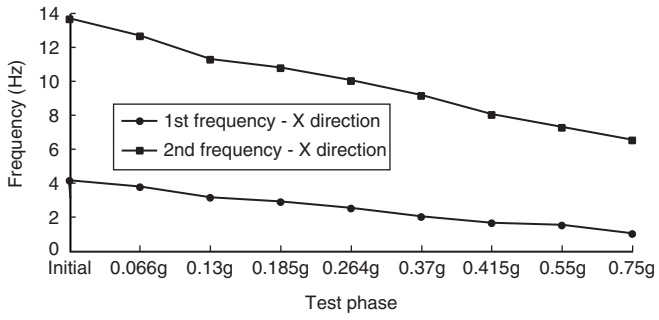

Figure 13. Variation of the first and second natural frequency

It can be seen from Figure 14 that the damping ratio increases as the frequency decreases whereas the stiffness ratio decreases. After the test phase with PGA of 0.185 g, the frequency reduced to 2.875 Hz and the damping ratio increased relatively rapidly, especially after the 0.370 g test phase, because the structure stepped into an inelastic stage. It helps reduce the energy of seismic input at a faster rate than the reduction in stiffness, so the structure will be safe in a strong earthquake. The model then simply readjusted itself to oscillate in an elastic manner around new equilibrium position having a reduced stiffness and an increased damping with a certain frequency as shown in Figure 14. For an example, the initially equilibrium position is verified with the first natural frequency of 4.125 Hz and corresponding with the damping ratio of 0.040. After the test phase with PGA of 0.066 g, the equilibrium position is verified with the first natural frequency of 3.750 Hz and corresponding with the damping ratio of 0.051 and stiffness ratio of 0.826 and so on. However, from the test phase with PGA of 0.185 g, the damage was visible and the damaged model was continuously carried out with higher PGAs. Therefore, the existed damaged of the model caused influences on the natural frequency of the model. It can be considered that the model tested (from PGAs of 0.185 g) has a higher damping ratio than that of the initial model. It is likely to cause the reduction of frequency compared to the result if it would be obtained from test on the initial model.

Table 4. Natural frequency, damping ratio and stiffness ratio in the X-direction

PGA (g)	Initial	0.066	0.130	0.185	0.264	0.370	0.415	0.550	0.750
1st Frequency (Hz)	4.125	3.75	3.125	2.875	2.50	2.125	1.75	1.625	1.00
2nd Frequency (Hz)	13.625	12.625	11.25	10.75	9.875	9.125	8.00	7.25	6.75
Damping ratio	0.040	0.051	0.060	0.055	0.096	0.192	0.234	0.330	0.451
Stiffness ratio	1	0.826	0.574	0.486	0.367	0.235	0.155	0.132	0.059

The first two vibration modes in the X-direction are shown in Figure 15. It can be seen that the lateral stiffness uniformly distributes along the height and the first-order vibration mode shows a shear-type feature. The results show that the natural frequencies, stiffness ratios and damping ratios gradually change as the amplitude of earthquake inputs increase gradually.

4.3. Acceleration Amplification

The acceleration amplification was determined by dividing the maximum response acceleration measured on each floor by an input PGA during each test phase. As shown in Figure 16, the acceleration amplifying coefficient gradually increases along the height under the same earthquake level and decreases as the PGA of excitations increases due to the progressive degradation of structural stiffness. This distribution feature is more obviously seen from the test phases with PGAs from 0.066 g to 0.185 g. The influence of high-order vibration modes increases after the test phase with PGA of 0.370 g so the acceleration amplifying coefficient is no more conforming with that distribution. The maximum acceleration amplifying coefficient obtained during these test phases was 4.587 at 6th floor for the ELW with PGA of 0.066 g.

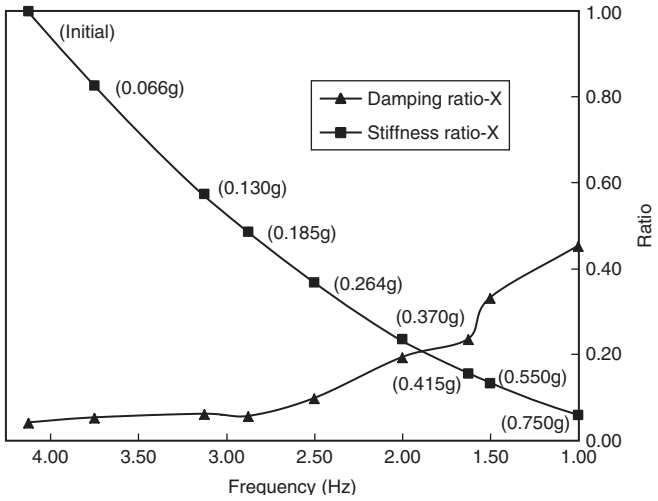

Figure 14. Damping and stiffness ratio vs. frequency in X-direction

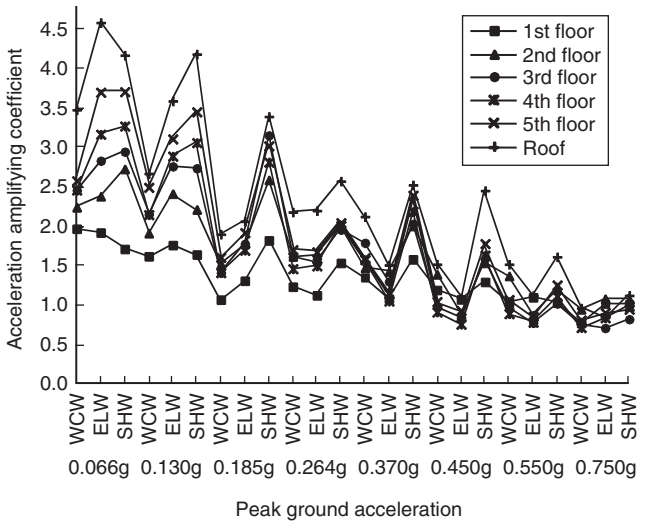

Figure 16. Distribution of acceleration amplifying coefficient in X-direction

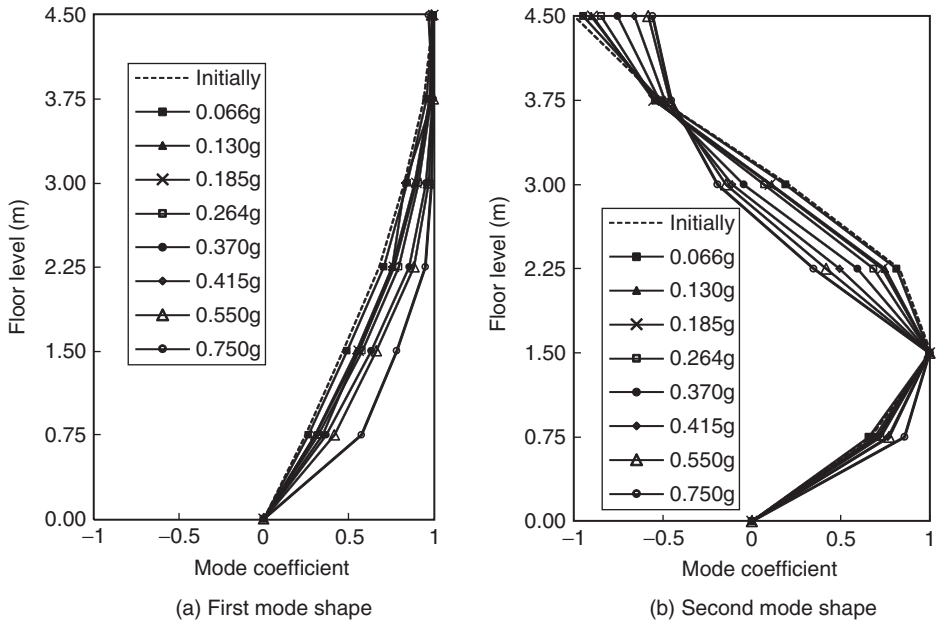

Figure 15. First and second mode shapes in X-direction

4.4. Earthquake Action

The seismic forces were calculated based on the mass distribution at each floor and the measured accelerations at the measurement points on each floor of the model structure. The maximum seismic force of i^{th} floor is derived as follows:

$$F_{i,\max} = m_i \left| \{\ddot{x}_i(t) + \ddot{x}_0(t)\}_{\max} \right| \quad (3)$$

where, $F_{i,max}$ is the maximum seismic force of the i^{th} floor; m_i is the lumped mass of the i^{th} floor; $\ddot{x}_i(t)$ is the relative acceleration response of the i^{th} floor at the time of t; and $\ddot{x}_0(t)$ is the ground acceleration at the time of t; $\{\ddot{x}_i(t) + \ddot{x}_0(t)\}$is the absolute acceleration response of i^{th} floor of the frame model at the time of t;

Figure 17 describes the distribution of the maximum seismic force in the X-direction. From the figure, it can be seen that the distribution of the maximum seismic force is accepted to the inverted triangular form along the height during the test phases with PGAs from 0.066 g to 0.130 g, and the seismic force increases progressively with the gradually increasing acceleration amplitude. Since the test phase with PGA of 0.185 g, the influence of high-order vibration modes develops and consequently the inverted triangular form is not appropriate any more for the distribution of the maximum seismic force. The maximum seismic force obtained during these test phases was 21.679 kN at 6th floor for the SHW with PGA of 0.415 g. Although the PGAs of the later test phases were greater, the maximum seismic forces were all smaller than that of SHW with PGA of 0.415 g as shown in Figure 16(c). This trend is followed under WCW, after reaching the highest value of 18.43 kN at 2nd floor with PGA of 0.550 g, the seismic forces decrease while PGAs increase as shown in Figure 17(a).

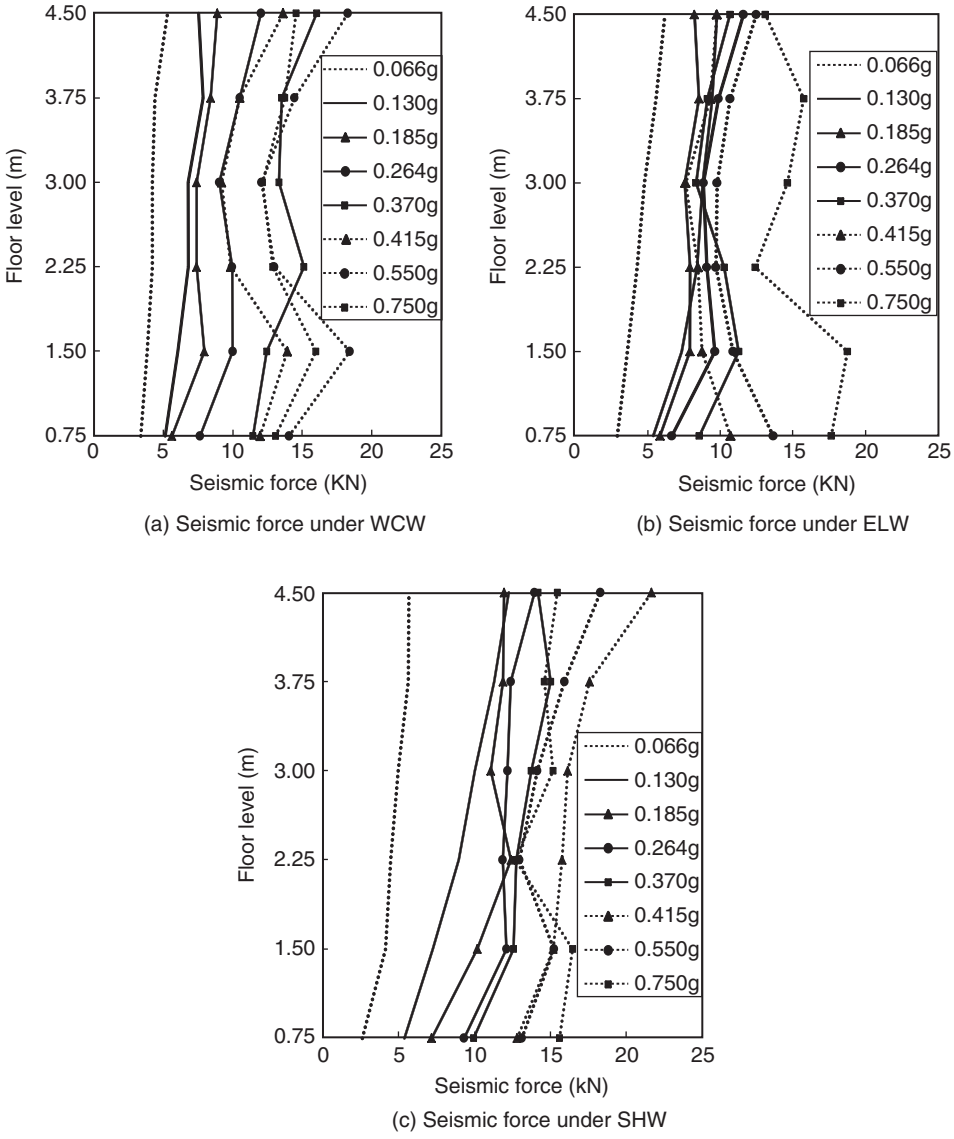

Figure 17. Distribution of seismic force in X-direction

However, the seismic force under ELW inputs behaves differently as shown in Figure 17(b). During the test phase with PGA of 0.066 g, the distribution presents a quite linear increase and then the seismic force increases relatively slowly during the later test phases. However, the test phase with PGA of 0.750 g reveals that the seismic force dramatically increases.

Based on the three factors of primary importance determining the earthquake response of a structure, which are the type of framing, the mass distribution, and the relative contribution of the higher modes of vibration, it can be considered that the distribution of the maximum seismic force of the precast RAC model was mainly impacted not only by different seismic waves but also different higher modes under different input motions.

Structural story shear force is one of the important studying parameters in earthquake response analysis because it reflects the amount of seismic internal force. The values of story shear force were calculated based on the measured accelerations and the mass distribution at floors. The story shear is derived as follows:

$$V_i(t) = \sum_{j=i}^{n} F_i(t) = \sum_{j=i}^{n} m_j\{\ddot{x}_j(t) + \ddot{x}_0(t)\} . \quad (4)$$

where, $V_i(t)$ is the story shear force of i^{th} floor of the model structure at the time of t; $F_i(t)$ presents seismic force of i^{th} floor of the model at the time of t; m_j is the lumped mass of j^{th} floor of the frame model; $\{\ddot{x}_j(t) + \ddot{x}_0(t)\}$ is the absolute acceleration response of j^{th} floor of the frame model at the time of t; and n represents the total number of floors.

Figure 18 displays the distribution of the maximum story shear distribution in the X-direction. As shown in this figure, the maximum story shear reduces steadily along the height and the triangular form is appropriate

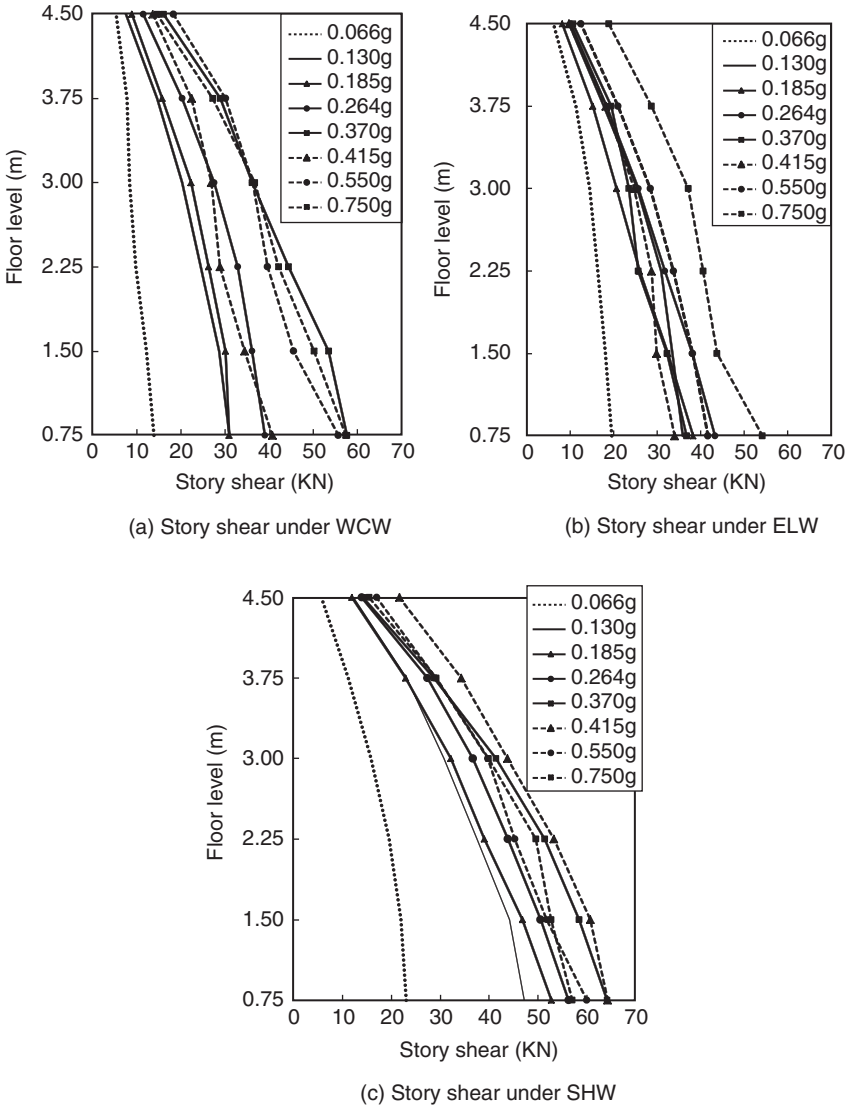

(a) Story shear under WCW

(b) Story shear under ELW

(c) Story shear under SHW

Figure 18. Distribution of story shear force in X- direction

for these distributions during the test phases with PGAs from 0.066 g to 0.130 g (elastic stage). In the later test phases (elastic-plastic stage), the variation trend is partly affected by high-order vibration modes so the distributions do not follow triangular form but still tend to reduce along the height.

Shear amplification factor β_Q can be calculated by following formula:

$$\beta_Q = \frac{|Q|_{\max}}{M \cdot |a|_{\max}}. \quad (5)$$

where, $|Q|_{\max}$ is the maximum absolute value of shear force of the first floor (base shear); M is the total mass of the model; and $|a|_{\max}$ is the maximum absolute acceleration of the shake table.

From Figure 19, the variation of shear amplification factor depends not only on amplitude of excitation but also on the type of earthquake waves. However, the shear amplification factor in general decreases in all types of earthquake waves. There is a rapid descent with ELW up to the test phase with PGA of 0.370 g, after that the shear

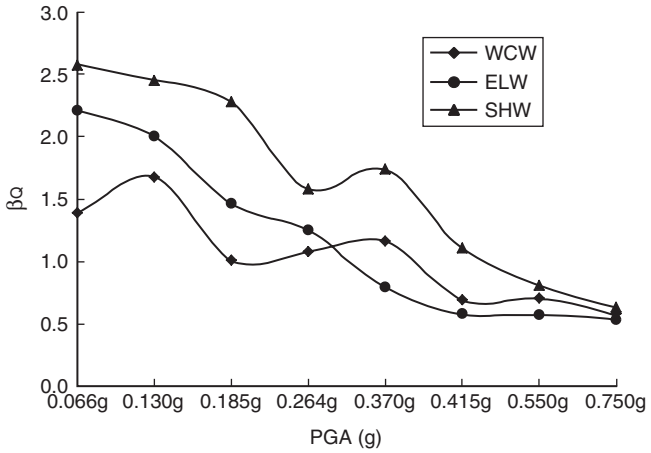

Figure 19. Variation of shear amplification factor

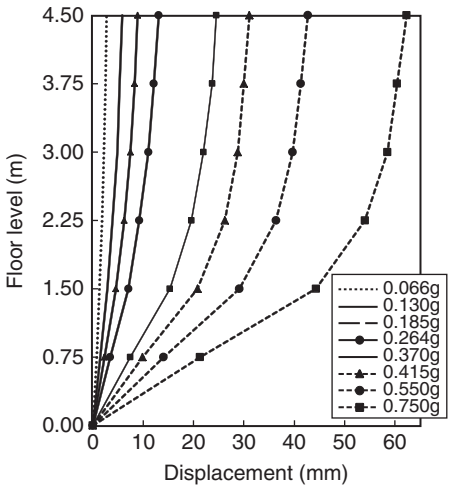

(a) Maximum story displacement under WCW

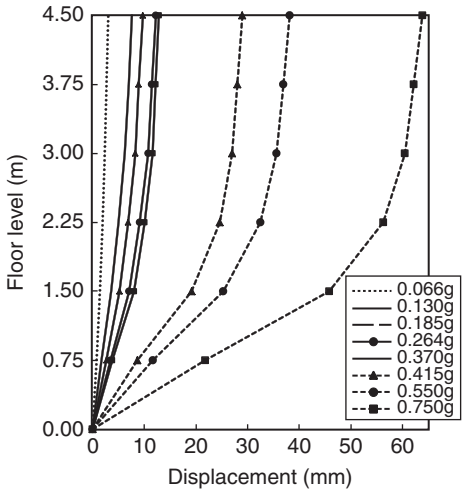

(b) Maximum story displacement under ELW

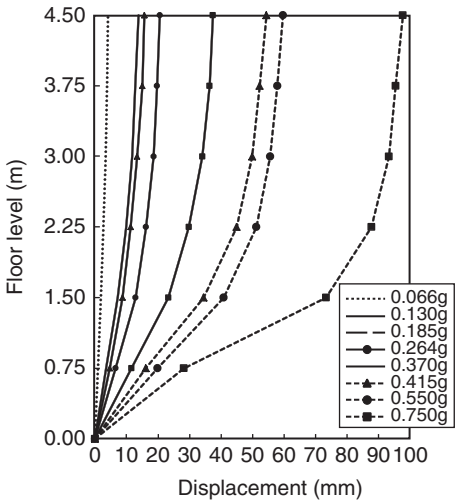

(c) Maximum story displacement under SHW

Figure 20. Maximum story displacement of the precast RAC model in X- direction

amplification factor decreases more slowly. Meanwhile, the shear amplification factors under WCW and SHW show a similar trend in the shape of a wave. After the test phase with PGA of 0.415 g, the difference of shear amplification factors among three seismic waves is small and mostly converges in the final test phase.

4.5. Deformation

LVDTs were installed on each floor to monitor the lateral displacement response. In order to investigate the structural deformation response under different earthquake levels, the maximum story displacements obtained were illustrated and the maximum story drift distributions along the height were also demonstrated as shown in Figs. 20 and 21, respectively.

It is clearly seen from Figure 20 that the curves of the maximum story displacement in all types of earthquake waves show a shear-type distribution feature. Compared with WCW and ELW, the maximum story displacement of 97.76 mm caused by SHW is the largest relative displacement. Generally, the maximum story displacement curves are relatively smooth without inflexions, which means that the distribution of equivalent rigidities along the height of the structure is well proportioned. Structural deformation curves are similar in shape with the first-order vibration mode shown in Figure 15 for the precast RAC frame structure.

Figure 21 shows the shape of the maximum inter-story drift curves which is similar in all three types of earthquake wave. There is a slow rise in the maximum inter-story drift until the test phase with PGA of 0.370 g was carried out, but after that the maximum inter-story drift increases more rapidly. For all of the test phases, the maximum inter-story drift of the second floor is bigger than that of all other floors under the same earthquake level. The maximum inter-story drift of the second floor reached 1/17 (45.131/750) in the final test phase caused by SHW because the precast RAC frame model undergone a large deformation during this test phase.

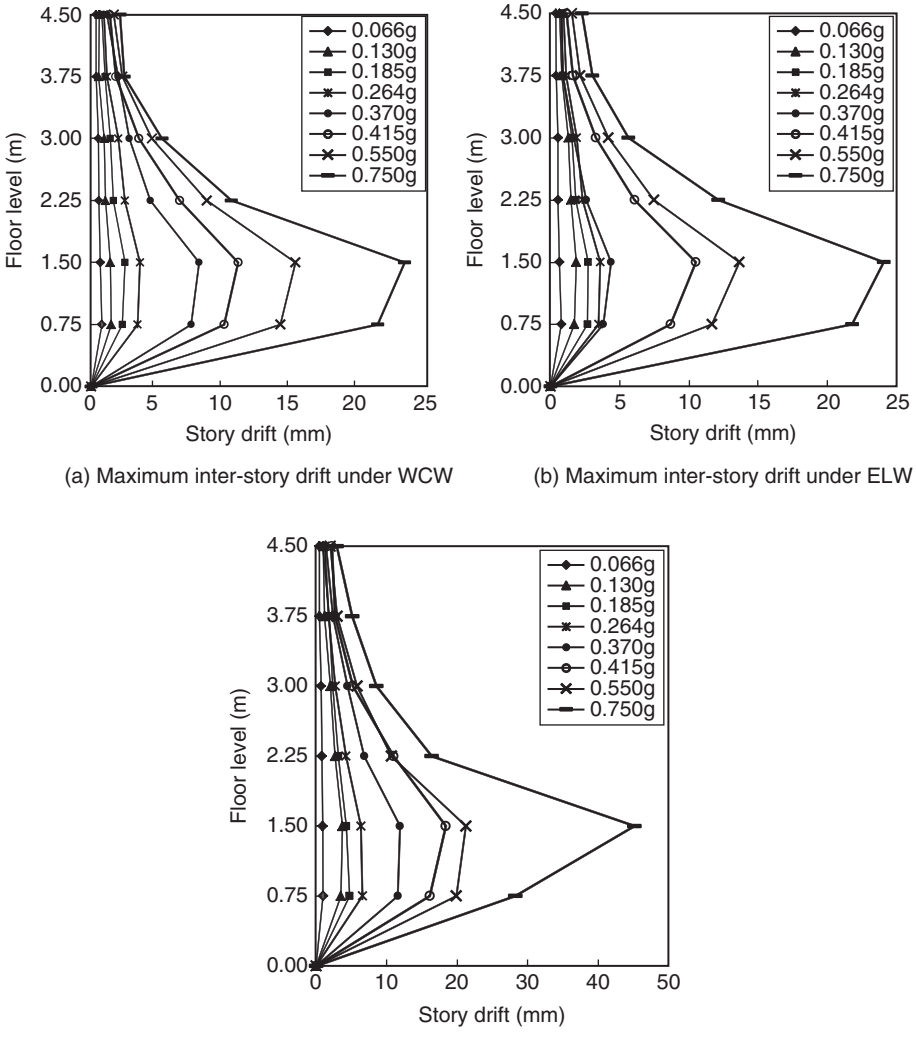

(a) Maximum inter-story drift under WCW

(b) Maximum inter-story drift under ELW

(c) Maximum inter-story drift under SHW

Figure 21. Maximum inter-story drift of the precast RAC model in X- direction

4.6. Hysteretic and Capacity Curves

Based on the results of the roof displacement and the total base shear force in the X-direction of the precast RAC frame model, the hysteretic curves of the overall structure obtained under the test phases of SHW are shown in Figure 22.

The relation between base shear forces and the roof displacements is linear during the test phase with PGA of 0.066 g. Then the lateral stiffness of the model structure degenerates slightly during the test phase with PGA of 0.130 g indicating that the RAC frame model structure is stepping into an elastic-plastic range.

The pinching phenomenon is slightly observed during the phase with PGA of 0.185 g. The lateral stiffness of the model degrades significantly during the test phase caused by SHW with PGA of 0.370 g and the pinching phenomenon can be recognized. The maximum base shear of the model is close to the maximum load bearing capacity of the structure in the test phase with PGA of 0.415 g. The pinching effect on the hysteric curves is more obvious in the later test phases because of shear deformations. However, the hysteretic curves perform somewhat disorderly; also it still reveals the stiffness and strength deterioration of the precast RAC frame structure under the final test phase as shown in Figure 22.

It is noted that from the test phase with PGA of 0.185g, the damage was visible and the damaged model was continuously carried out with higher PGAs. It can be considered that the model tested (from PGAs of 0.185g) has a higher damping ratio than that of the initial model. It is likely to cause the increase of energy dissipation which was represented by hysteresis loops.

The form of exponential function for the base shear was selected to express the capacity curve of the precast RAC frame model as obtained in the following formula and drawn in Figure 23.

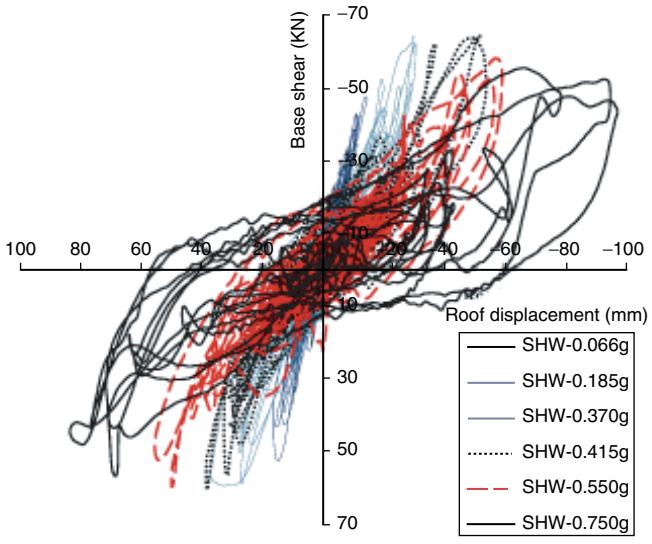

Figure 22. Hysteretic curves of the precast RAC model

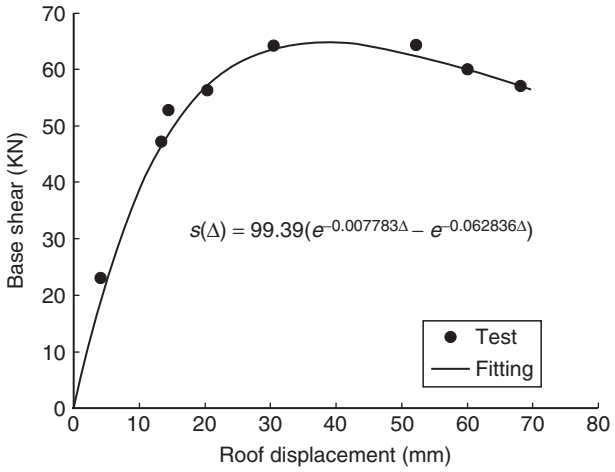

Figure 23. Capacity curve of the precast RAC model

$$S(\Delta) = 99.39(e^{-0.007783\Delta} - e^{-0.062836\Delta}) \tag{6}$$

where, $s(\Delta)$ is the base shear (kN); and Δ is the roof displacement (mm).

The capacity curve reflects the variation of the load bearing capacity of the structure, and the slope of the curve visually reveals the change of the lateral stiffness of overall frame structure. Based on Eqn 6, the ductility of the precast RAC model can be evaluated through the definition of the feature points as described in the following section.

4.7. Displacement Ductility

$$\mu = \frac{\Delta_u}{\Delta_y}, \tag{7}$$

where, Δ_y is the yield lateral displacement; Δ_u is the lateral displacement when the load P_u falls to 85% of the maximum load P_m on the capacity curve; P_y is the lateral load corresponding to the yield lateral displacement Δ_y; K_0 is the initial lateral stiffness on the capacity curve as shown in Figure 23 .

According to the capacity curve shown in Figure 23 and Eqn 6, the values of feature points are calculated. It is noticed that the yielding point is determined thanks to the cracking point C as described in Figure 23. In addition, the value of $0.85P_m$ is smaller than the capacity of the structure at the final test phase. Therefore, the ultimate roof displacement was taken equal to 68.11 mm, which was corresponding to the maximum base shear of the structure observed in the test phase with PGA of 0.750 g. Then, the ultimate capacity of the structure P_u was recalculated from Eqn 6 which is equal to 57.11 kN as shown in Table 5.

Table 5. Values of feature points on the capacity curve

Yield Load P_y (kN)	Yield displacement Δ_y (mm)	Maximum load P_m (kN)	Ultimate Load P_u (kN)	Displacement corresponding to P_u Δ_u (mm)	Initial stiffness K_0 (kN/mm)
53.89	17.68	64.82	57.11	68.11	5.47

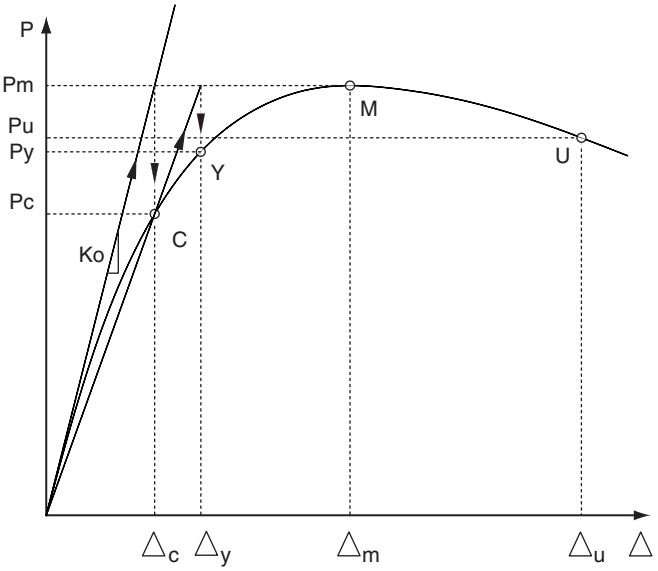

Figure 24. Definition of feature points on capacity curve

Finally, the ductility ratio is determined as 3.852 by Eqn 7. It is reveals that the precast RAC frame model has a good capacity to undergo deformation after its initial yield without any significant reduction in loading capacity. It also proves the enough aseismic capacity of the precast RAC frame structure.

5. CONCLUSIONS AND SUGGESTIONS

With a critical analysis on the seismic response of the precast RAC frame based on the shake table test results, some conclusions and suggestions are presented in the following:

(1) The cracking propagation and failure pattern of the precast Recycled Aggregate Concrete (RAC) model indicate that all precast RAC components of the structure work together well thanks to CIP joints. The crack pattern of joints in precast frame made of RAC is relatively similar to that of precast frame made of NAC.

(2) Throughout the shaking table test, the natural frequency and stiffness ratio gradually decrease with the increase of amplitude of the seismic waves. The damping ratio increases relatively quickly in the later test phases, which refers to a high energy-dissipating capacity frame structure when stepped into the plastic stage.

(3) The seismic responses including acceleration amplifying coefficient, seismic force and base shear show the distributions with the recognized rules along the height of the model in the elastic stage. Since 0.185 g test phase the distributions of those seismic responses were influenced by higher-order vibration modes. The curves of the maximum story displacement under all types of earthquake waves show a shear-type distribution feature.

(4) The capacity curve reveals good seismic behavior with a ductility coefficient of 3.852 and the reduction in lateral stiffness without any abrupt changes associated with sufficient load bearing capacity. Although some joints cracked, satisfactory hysteretic behavior was obtained. The result indicates that the CIP joints between precast RAC elements will supply sufficient shear capacity and ensure a certain level of seismic resistance.

(5) The good seismic resistance of the model has been convectively proved by the results of the shaking table test and a further report on analysis and evaluation of seismic performance of the precast RAC frame structure will be devoted to enhance the emulation of such kind of precast frame. Therefore, the construction process and designing of this study could be considered as a reference to earthquake resistance of precast frame structures made of RAC.

ACKNOWLEDGMENTS

This work was sponsored by the National Natural Science Foundation of China (51325802) and Shanghai Urban Construction Materials Co. Ltd. Special thanks are given to the State Key Laboratory for Disaster Reduction in Civil Engineering at Tongji University.

REFERENCES

Alcocer, S.M, Carranza, R., Navarrete, D.P. and Martinez R (2002). "Seismic tests of beam-to-column connections in a precast concrete frame", *PCI Journal*, Vol. 47, No. 3, pp. 70–89.

Andreas, S., Benson, S., and Joel, C. (2010). "Design, scaling, similitude, and modeling of shake-table test structures", *Shake Table Training Workshop 2010* – San Diego, CA, USA.

Andrzej, A. (2011). "Long-term behaviour of reinforced-concrete beams and columns made of recycled aggregate concrete", *Symposium PRAGUE 2011*, Czech.

Bhikshma, V. and Kishore, R. (2010). "Development of stress-strain curves for recycled aggregate concrete", *Asian Journal Civil Engineering (Building and Housing)*, Vol. 11, No. 2, pp. 253 –261.

Buckingham, E. (1914). "On physically similar system", *Physical Review*, Vol. 4, No. 4, pp. 345–376.

Corinaldesi, V. (2011). "Behaviour of beam–column joints made of recycled-aggregate concrete under cyclic loading", *Construction and Building Materials*, Vol. 25, pp. 1877 –1882.

Elwood, K.J., Pampanin, S. and Kam, W.Y. (2012). "22 February 2011 Christchurch Earthquake and implications for design of concrete structures", *Proceedings of the International Symposium on Engineering Lessons Learned from the 2011 Great East Japan Earthquake,* Tokyo, Japan, pp. 1157–1168.

Ericson, A.C. (1994). "Emulation design of precast concrete", *The Construction Specifier*, Vol. 47, No. 10, pp. 96 –103.

Ericson, A.C. and Warnes, C.E. (1990). *Seismic Technology for Precast Concrete Systems*, Concrete Industry Bulletin, Concrete Industry Board, Inc., Spring, USA.

Fonseca, N. (2011). "The influence of curing conditions on the mechanical performance of concrete made with recycled concrete waste", *Cement & Concrete Composites*, Vol. 33, pp. 637 –643

Limbachiya, M.C. (2004). "Performance of recycled aggregate concrete", *RILEM International Symposium on Environent-Consciuos Material and Systems for Sustainable*, Japan.

Lo, C.Y. (2008). "Comparison of recycled and natural aggregate properties", *The 3rd ACF International Conference-ACF/VCA*, Chiang Mai, Thailand.

550.1R-09 (2001). *Emulating Cast-in-Place Detailing in Precast Concrete Structures*, American Concrete Institute, USA.

Nakaki, S.D., Staton, J.F. and Sritharan, S. (1999). "An overview of the PRESSS five story precast test building", *PCI Journal*, Vol. 44, No. 2, pp. 28 –39.

Park, R. (1986). "Seismic design considerations for precast concrete construction in seismic zones", *Seminar on Precast Concrete Construction in Seismic Zones,* Japan Society for the Promotion of Science - United States National Science Foundation, Tokyo, pp. 1–38.

Parekh, D.N. and Modhera, C.D. (2011). "Characterization of recycled aggregate concrete", *International Journal of Advanced Engineering Technology*, Vol. 2, No. 4, pp. 321 –330.

Shariatmadar, H. and Beydokhti, E.Z. (2011). "Experimental investigation of precast concrete beam to column connections subjected to reversed cyclic loads", *6th International Conference on Seismology and Earthquake Engineering*, Tehran, Iran.

Shutt, C.A. (1995). *Precast Concrete Withstands Kobe Earthquake Tragedy*, In the News, Ascent Spring, pp. 32–36.

Xiao, J.Z., Sun, Y.D. and Falkner, H. (2006). "Seismic performance of frame structures with recycled aggregate concrete", *Engineering Structures*, Vol. 28, No. 1, pp. 1–8.

Xiao, J.Z., Tawana, M.M. and Wang, P.J. (2010). "Test on the seismic performance of frame joints with pre-cast recycled concrete beams and columns", *Proceedings of the 2nd International Conference on Waste Engineering and Management*, Shanghai, China, pp. 773–786.

Xiao, J.Z., Li, W.G., Fan, Y.H. and Huang, X. (2012). "An overview of study on recycled aggregate concrete in China (1996–2011)", *Construction and Building Materials*, Vol. 31, pp. 364 –383.

Xiao, J.Z., Pham, L., Wang, P.J. and Gao, G. (2014). "Behaviors of semi-precast composite beams made with recycled aggregate concrete", *Structural Design of Tall and Special Buildings*, Vol. 23, pp. 692–712.

Xue, W.C and Yang, X.L (2010). "Seismic tests of precast concrete, moment-resisting frames and connections", *PCI Journal*, Vol. 55, No. 3, pp. 102–121.

Zhang, L., Zhang, X. and Yan, G. (2006). "Experimental research on the shearing capacity of recycled aggregate concrete beams without stirrups" *Journal of Zhengzhou University (Engineering Science)*, Vol. 27, pp. 18–23. (in Chinese)

Zhou, J.H., Wang, X.B. and Yu, T.H. (2008). "Mechanic behaviour test on recycled concrete simply-supported rectangular slabs", *Journal of Shenyang Jianzhu University (Natural Science Edition)*, Vol. 4, No. 3, pp. 411–415. (in Chinese)